

# Rotation of an atomic Bose-Einstein condensate with and without a quantized vortex

I. Corro, N. G. Parker and A. M. Martin

School of Physics, University of Melbourne, Parkville, VIC 3010, Australia

## Abstract.

We theoretically examine the rotation of an atomic Bose-Einstein condensate in an elliptical trap, both in the absence and presence of a quantized vortex. Two methods of introducing the rotating potential are considered - adiabatically increasing the rotation frequency at fixed ellipticity, and adiabatically increasing the trap ellipticity at fixed rotation frequency. Extensive simulations of the Gross-Pitaevskii equation are employed to map out the points where the condensate becomes unstable and ultimately forms a vortex lattice. We highlight the key features of having a quantized vortex in the initial condensate. In particular, we find that the presence of the vortex causes the instabilities to shift to lower or higher rotation frequencies, depending on the direction of the vortex relative to the trap rotation.

PACS numbers: 03.75.Lm, 03.75.Kk

## 1. Introduction

Due to their superfluid nature, dilute atomic Bose-Einstein condensates (BECs) are constrained to rotate only through the presence of vortices with quantized angular momentum [1]. In analogy to the rotating bucket experiment in liquid Helium [2], rotation of a dilute BEC can lead to the nucleation of vortices. The onset of vortex nucleation in a rotating condensate is non-trivial and has been the subject of much experimental [3, 4, 5, 6, 7, 8] and theoretical [1, 9, 10, 11, 12, 13, 14, 15, 16, 17, 18, 19, 20, 21] investigation. One method of spinning the condensate is to use a rotating elliptical harmonic trap, with the presence of vortices predicted to become energetically feasible for rotation frequencies exceeding  $\Omega \sim 0.3\omega_{\perp}$  [9], where  $\omega_{\perp}$  is the average trap frequency in the rotating plane. Experimentally, however, vortices are formed only when the trap is rotated at much higher frequencies [3, 4, 5]. This anomaly exists because it is only at these higher frequencies that a dynamical route to vortex nucleation appears.

In the rotating frame, the static condensate solutions in an elliptical trap are a family of quadrupole solutions with elliptical density profiles. These solutions, and their regimes of stability, can be conveniently approximated using the classical hydrodynamic equation in the rotating frame [12, 13]. Experimentally, these solutions can be accessed by two methods: Procedure I involves increasing the rotation frequency from zero while maintaining a fixed elliptical trap, while Procedure II involves increasing the trap ellipticity from zero while rotating at a fixed frequency. Providing these procedures are performed adiabatically, the condensate will access the

stationary states in the rotating frame. Indeed, this has been observed experimentally [5, 7]. However, depending on which procedure is employed, a critical rotation frequency/ellipticity is reached beyond which these vortex-free solutions become unstable and lead to the formation of a vortex lattice. The onset of the instability has been mapped out theoretically based on classical hydrodynamics [12, 13, 20] and is in excellent agreement with experimental results [5, 7]. Furthermore, time-dependent simulations of the highly-successful Gross-Pitaevskii equation [22] have elucidated the full dynamics of this process [14, 15, 16, 17, 18, 19, 20], including the non-trivial transition from instability to vortex lattice. If the rotating elliptical trap is introduced non-adiabatically, instead, the condensate undergoes shape oscillations which can be unstable and lead to vortex lattice formation. These non-adiabatic dynamics have been observed experimentally [7] and elucidated theoretically [14, 18, 19].

A natural extension of these studies is to consider how the presence of a quantized vortex in the initial condensate affects the dynamics under rotation. To date this has been considered by a handful of theoretical studies. The effect of a vortex on the collective modes of a condensate has been analysed [23, 24, 25, 26] and predicted to induce an upwards shift in the mode frequencies. Tsubota *et al.* [14] showed that a rotating condensate containing a vortex undergoes similar dynamics to the vortex-free case, although the final configuration of vortices depends on the initial state. Such hysteresis effects, depending on the initial angular momentum state of the condensate, have been studied in more detail by Jackson and Barenghi [21]. Crucially, these theoretical studies consider only the case of a vortex whose flow is concurrent with the trap rotation. In this paper we consider the rotation of a condensate containing a vortex whose flow is either concurrent or against the trap rotation. We examine the adiabatic introduction of the rotating elliptical trap, either by increasing the rotation frequency for a fixed trap ellipticity (Procedure I) or by increasing the trap ellipticity at fixed trap rotation frequency (Procedure II). We map out the onset of instability that triggers vortex lattice formation for both of these procedures, and compare to the non-vortex case.

In section 2 we outline our theoretical approaches, namely, the full time-dependent simulation of the condensate using the Gross-Pitaevskii equation and an analysis of the classical hydrodynamic solutions in the rotating frame. In section 3 we describe the instabilities of a vortex-free condensate that arise from introducing a rotating elliptical trap, and present new results. In particular, we make a thorough comparison between the analytic hydrodynamic predictions and the computational simulations of the Gross-Pitaevskii equation. In section 4 we examine how the presence of a vortex changes these dynamics, and, in particular, contrast the cases where the vortex flow is concurrent and against the rotating trap. Finally, in section 5 we present the conclusions of our investigation.

## 2. Theory

Assuming ultra-cold temperature and weak atomic interactions, the vast majority of the bosons in the system are in the Bose-condensed state. Thermal and quantum effects can become negligible and the condensate can be parameterised by a macroscopic “wavefunction”  $\psi(\mathbf{r}, t)$ . Moreover, this wavefunction is governed by the mean-field Gross-Pitaevskii equation (GPE). In the frame rotating at frequency

$\Omega$  about the  $z$ -axis this equation has the form,

$$i\hbar \frac{\partial \psi(\mathbf{r}, t)}{\partial t} = \left[ -\frac{\hbar^2}{2m} \nabla^2 + V_{\text{ext}}(\mathbf{r}, t) + g|\psi(\mathbf{r}, t)|^2 - \Omega \hat{L}_z \right] \psi(\mathbf{r}, t), \quad (1)$$

where  $V_{\text{ext}}(\mathbf{r}, t)$  is the external confinement and  $m$  is the atomic mass. The nonlinear coefficient  $g = 4\pi\hbar^2 Na/m$  characterises the atomic interactions, where  $N$  is the number of atoms and  $a$  is the  $s$ -wave scattering length. The term containing the angular momentum operator  $\hat{L}_z$  accounts for frame rotation about the  $z$ -axis. The GPE represents the back-bone of theoretical studies into BECs and has been shown to give an excellent description of many static and dynamical effects, including vortices [1, 22].

### 2.1. Hydrodynamic approach

It is useful to consider the hydrodynamic interpretation of the wavefunction  $\psi(\mathbf{r}, t) = \sqrt{\rho(\mathbf{r}, t)} \exp[i\phi(\mathbf{r}, t)]$ , where  $\rho(\mathbf{r}, t)$  is the atomic density and  $\phi(\mathbf{r}, t)$  is a phase factor which defines a fluid velocity via  $\mathbf{v}(\mathbf{r}, t) = (\hbar/m)\nabla\phi(\mathbf{r}, t)$ . Substitution of these relations into the GPE and equating real and imaginary parts leads to the classical hydrodynamic equations,

$$\frac{\partial \rho}{\partial t} + \nabla \cdot [\rho(\mathbf{v} - \boldsymbol{\Omega} \times \mathbf{r})] = 0, \quad (2)$$

$$m \frac{\partial \mathbf{v}}{\partial t} + \nabla \left( \frac{1}{2} m \mathbf{v} \cdot \mathbf{v} + V_{\text{ext}}(\mathbf{r}, t) + \rho g - m \mathbf{v} \cdot [\boldsymbol{\Omega} \times \mathbf{r}] \right) = 0. \quad (3)$$

Equation (2) is a continuity equation while equation (3) has the form of a Euler equation for an irrotational fluid. In deriving equation (3) we have employed the Thomas-Fermi approximation by neglecting the non-trivial ‘quantum pressure’ term  $\frac{\hbar^2}{2m} \frac{\nabla^2 \sqrt{\rho}}{\sqrt{\rho}}$  [12, 13, 20].

The confining potential  $V_{\text{ext}}(\mathbf{r}, t)$  is typically formed by magnetic fields and has the harmonic form,

$$V_{\text{ext}}(\mathbf{r}, t) = \frac{1}{2} m (\omega_x^2 x^2 + \omega_y^2 y^2 + \omega_z^2 z^2), \quad (4)$$

where  $\omega_x$ ,  $\omega_y$  and  $\omega_z$  are the harmonic trap frequencies in the three cartesian dimensions. In the experiments of [3, 5, 7] the trap is approximately elliptical in the rotating ( $x$ - $y$ ) plane. Therefore we employ an ellipticity parameter  $\epsilon$  to define the  $x$ ,  $y$  trap frequencies to be  $\omega_x = \sqrt{1 - \epsilon} \omega_{\perp}$  and  $\omega_y = \sqrt{1 + \epsilon} \omega_{\perp}$ , where  $\omega_{\perp}^2 = (\omega_x^2 + \omega_y^2)/2$  is the geometric mean of the frequencies.

Rotation of the elliptical trap tends to excite a quadrupolar mode in the condensate. Following Recati *et al.* [12], we assume an irrotational quadrupolar flow in the condensate defined by the velocity field [29],

$$\mathbf{v} = \alpha \nabla(xy), \quad (5)$$

where  $\alpha$  is the velocity field amplitude. It is important to note that  $\alpha$  is also proportional to the ellipticity of the condensate density profile. Following the analytic procedure in references [12, 13, 20], the classical hydrodynamics equations leads to a density profile given by,

$$\rho = \frac{1}{g} \left( \mu - \frac{1}{2} m (\tilde{w}_x^2 x^2 + \tilde{w}_y^2 y^2 + w_z^2 z^2) \right), \quad (6)$$

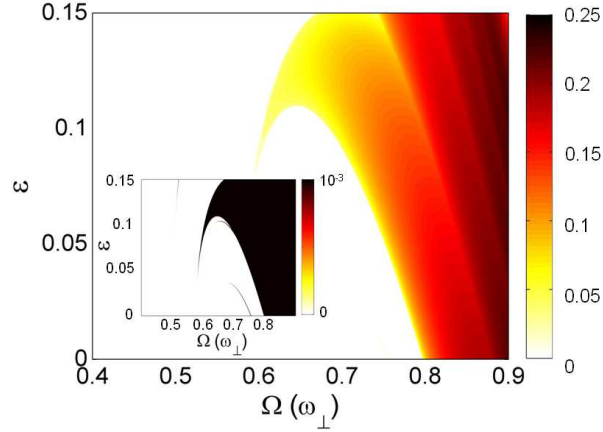


**Figure 1.** The size of the largest real part of eigenvalues found using equation (8). The size of the eigenvalue is indicative of the speed at which the condensate breaks down upon entering an unstable region. The inset shows the same plot but at much lower amplitude to highlight the unstable regions with small eigenvalues which are not visible in the main plot.

for  $\rho > 0$ , and  $\rho = 0$  elsewhere. Furthermore, this leads to the equation,

$$\alpha^3 + (1 - 2\Omega^2)\alpha - \epsilon\Omega = 0, \quad (7)$$

which defines the stationary condensate solutions (defined by the quadrupolar flow amplitude  $\alpha$ ) in a harmonic trap with ellipticity  $\epsilon$  rotating at frequency  $\Omega$ . Throughout this paper we will consider the relevant parameter space  $(\epsilon - \Omega)$  which defines these condensate solutions.

Although equation (7) defines static solutions, they are not necessarily *stable* solutions. To examine their dynamical stability, we consider small perturbations in density  $\delta\rho$  and phase  $\delta\phi$  to the static solutions [13, 20]. Taking the variational derivatives of equations (2) and (3) leads to the time-evolution equations

$$\frac{\partial}{\partial t} \begin{bmatrix} \delta\phi \\ \delta\rho \end{bmatrix} = - \begin{bmatrix} \mathbf{v}_c \cdot \nabla & g/\hbar \\ \nabla \cdot (\rho_0 \frac{\hbar}{m} \nabla) & \mathbf{v}_c \cdot \nabla \end{bmatrix} \begin{bmatrix} \delta\phi \\ \delta\rho \end{bmatrix} \quad (8)$$

where  $\mathbf{v}_c = \mathbf{v} - \boldsymbol{\Omega} \times \mathbf{r}$  is the velocity field in the rotating frame. A polynomial ansatz is taken for the perturbations  $\delta\rho$  and  $\delta\phi$ , and inserted into equation (8). As a technical note, our polynomial ansatz consists of terms of the form  $x^i y^j$ , where  $i, j \geq 0$  and  $i + j \leq 7$ . If the resulting eigenvalues are purely imaginary (or contain a negative real part) then the perturbations are stable oscillations (or decay over time). However, if any of the eigenvalues have a real positive component, the perturbations will grow exponentially over time. Such solutions are dynamically unstable and lead to vortex lattice formation [13, 20].

Equation (8) defines regions in  $(\epsilon - \Omega)$  space that are unstable as shown in figure 1. When the ellipticity and rotation frequency of the trap enters this region the instability leads to disruption of the condensate, vortex nucleation and ultimately lattice formation. The speed at which the instability evolves will increase with the size of the real part of the eigenvalues. The size of the largest real component of the eigenvalues are mapped out in figure 1. This shows that some regions of instability will

take significantly longer to produce vortices than others. This effect will also be studied in detail in section 3.

Another source of instability to consider is the center of mass instability which occurs when the rotation frequency becomes close to the trapping frequency [12]. This instability is equivalent to the classical case of a point particle in a rotating elliptical potential. For rotation frequencies  $\Omega$  lying between  $\tilde{\omega}_x$  and  $\tilde{\omega}_y$  the oscillations of the trapping potential couple to the oscillation frequencies of the particle and it is ejected from the trap. This has been experimentally observed in the explosion of the condensate [27]. However, for sufficiently strong repulsive interactions, explosion is prevented and the condensate remains intact, although its centre of mass deviates from the trap centre [19, 27].

## 2.2. Numerical solution of the GPE

Although the hydrodynamic approach outlined above gives valuable insight into the rotating condensate solutions, it has limitations. For example, it assumes the Thomas-Fermi limit, it can only predict the stability of modes with known flow patterns, and it cannot give information about how the instability manifests itself or the final state of the system. A more thorough method, albeit more intensive, is to explicitly solve the full Gross-Pitaevskii equation. Importantly, this method allows us to simulate the time dynamics of the condensate from the initial state all the way to its final state.

We employ the Crank-Nicholson method to numerically propagate the Gross-Pitaevskii equation in time. The dynamics predicted by equations (5) and (8) are independent of  $z$  [13, 20] so we are justified in conducting the simulations in two-dimensions. Condensate solutions are found by the imaginary-time technique. Under the substitution ( $t \rightarrow -it$ ) and using an appropriate initial guess, the GPE converges to the lowest energy solution of the system, provided it is stable [31].

In presenting our numerical results, we employ the healing length  $\xi = \hbar/\sqrt{mn_0g}$  as the unit of length and  $(\xi/c)$  as the unit of time, where  $n_0$  is the peak condensate density of the initial (non-rotating) solution and  $c = \sqrt{n_0g/m}$  is the Bogoliubov speed of sound. The chemical potential  $\mu = n_0g$  at  $t = 0$  is the unit of energy. We consider a condensate with  $\mu = 7\hbar\omega$  and a Thomas-Fermi radius of  $R_{\text{TF}} = 10\xi$ . Assuming  $^{87}\text{Rb}$  atoms, our units of space and time typically correspond to  $\xi \sim 0.2 \mu\text{m}$  and  $(\xi/c) \sim 10^{-4}$  s.

Once the solutions are found, they are propagated with the GPE in real time. We follow the experimental procedures as closely as possible [3, 5, 7]. We first obtain the initial solution with either  $\Omega = 0$  or  $\epsilon = 0$  and then introduce the rotating elliptical trap adiabatically by following Procedure I or Procedure II. The condition of adiabaticity is important because it means that the evolving condensate will access the rotating frame solutions. The non-adiabatic introduction of the rotating elliptical trap leads, instead, to oscillations between a non-elliptical and elliptical state [18, 19].

Recent numerical studies [18, 19, 20] have highlighted the necessity of rotational symmetry breaking for successful and realistic vortex nucleation. For example, if the two-fold rotational symmetry of the system is preserved then vortices must enter in opposing pairs, which is highly unfavourable in energetic terms. Consequently, at the start of each simulation of the GPE we shift the trap centre by a distance of  $0.1\xi$ . This breaks the two-fold rotational symmetry of the system and enables realistic vortex nucleation.

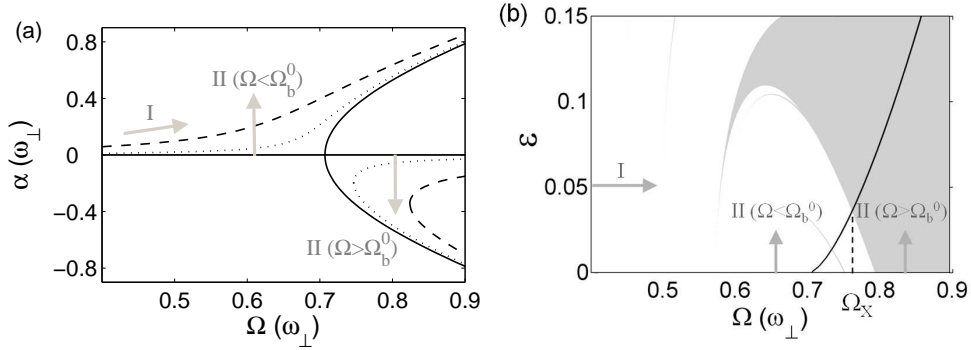


**Figure 2.** (a) Hydrodynamic quadrupole condensate solutions  $\alpha$  of the rotating condensate as a function of rotation frequency according to equation (7) for  $\epsilon = 0$  (solid line),  $\epsilon = 0.02$  (dotted line) and  $\epsilon = 0.1$  (dashed line). (b) The position of the bifurcation point  $\Omega_b(\epsilon)$  (solid line) and the unstable region (grey area) of the hydrodynamic condensate solutions are indicated. The crossing frequency  $\Omega_X$  is shown. In both (a) and (b), the routes for introducing the rotating elliptical trap, Procedure I and II, are illustrated. For Procedure II, rotation in the regime  $\Omega < \Omega_b^0$  accesses the upper branch of the solutions, while rotation in the regime  $\Omega > \Omega_b^0$  accesses the lower branch.

### 2.3. Energy of a rotating condensate

In the laboratory frame the energy is not conserved due to the presence of the time-dependent potential. The energy in the rotating frame is conserved (providing no dissipation is present) and is given by,

$$E = \int \left[ \frac{\hbar^2}{2m} |\nabla\psi|^2 + V_{\text{ext}}|\psi|^2 + \frac{g}{2} |\psi|^4 \right] dx dy - \Omega_z \langle \hat{L}_z \rangle, \quad (9)$$

The terms in the integral represent the kinetic energy  $E_K$ , potential energy  $E_P$  and interaction energy  $E_I$ . The final term represents the rotational energy, where the average angular momentum per particle about the  $z$ -axis,  $\langle \hat{L}_z \rangle$ , is given by,

$$\langle \hat{L}_z \rangle = \int \left[ -i\hbar \left( x \frac{\partial\psi}{\partial y} - y \frac{\partial\psi^*}{\partial x} \right) \right] dx dy, \quad (10)$$

### 3. Rotating a vortex-free condensate

The instability of a vortex-free condensate under the adiabatic introduction of a rotating elliptical trap has been mapped out by experiment [5, 7] and theory [12, 13, 16, 20]. We will outline the key features of these studies, before presenting additional results. We generally consider the frequency regime  $\Omega < \omega_\perp$ . Above this frequency, centrifugal forces overcome the trap potential and the condensate can undergo explosion or centre-of-mass oscillations [12, 19, 27].

Figure 2(a) shows the static solutions in  $(\alpha - \Omega)$  space according to equation (7). It should be recalled that  $\alpha$  defines the condensate solution via equation (5) and is proportional to the ellipticity of the BEC density profile. For an axially-symmetric trap  $\epsilon = 0$  (solid line), the  $\alpha = 0$  solution exists throughout while for  $\Omega > \omega_\perp/\sqrt{2}$  two additional solutions bifurcate symmetrically to finite negative and positive values of

$\alpha$ . We denote the frequency of this bifurcation point to be  $\Omega_b^0$ . For finite  $\epsilon$  [dashed and dotted lines in figure 2(a)] there exist two distinct branches of solutions. The upper branch of  $\alpha$  is positive, single-valued and occurs for all rotation frequencies. The lower branch is negative, double-valued, and only exists for  $\Omega > \Omega_b(\epsilon)$ . The bifurcation frequency  $\Omega_b(\epsilon)$  is now a strict function of ellipticity and increases with  $\epsilon$  as plotted in  $(\epsilon - \Omega)$  in figure 2(b) (solid line).

In addition to the static solutions, we also need to consider their dynamical instability according to equation (8). This predicts that the condensate solutions are dynamically unstable within a region of  $(\epsilon - \Omega)$  space, as shown by the shaded area in figure 2(b). As  $\epsilon$  is increased, the critical rotation frequency for dynamical instability becomes lower than  $\Omega_b(\epsilon)$ . We define the frequency at which these instabilities cross to be the crossing frequency  $\Omega_x = 0.765\omega_\perp$ .

We are now in a position to predict the behaviour of the condensate as a rotating elliptical trap is introduced, with the results presented below.

### 3.1. Procedure I

From the hydrodynamic point of view, the trap initially has fixed ellipticity, e.g.  $\epsilon = 0.1$  (dashed line in figure 2(a)). As the rotation frequency  $\Omega$  is increased from zero, the condensate follows the upper branch solution, becoming increasingly elongated as it moves to higher values of  $\alpha$ . As the BEC moves horizontally across figure 2(b), it becomes dynamically unstable when it reaches the unstable region (shaded region of figure 2(b)).

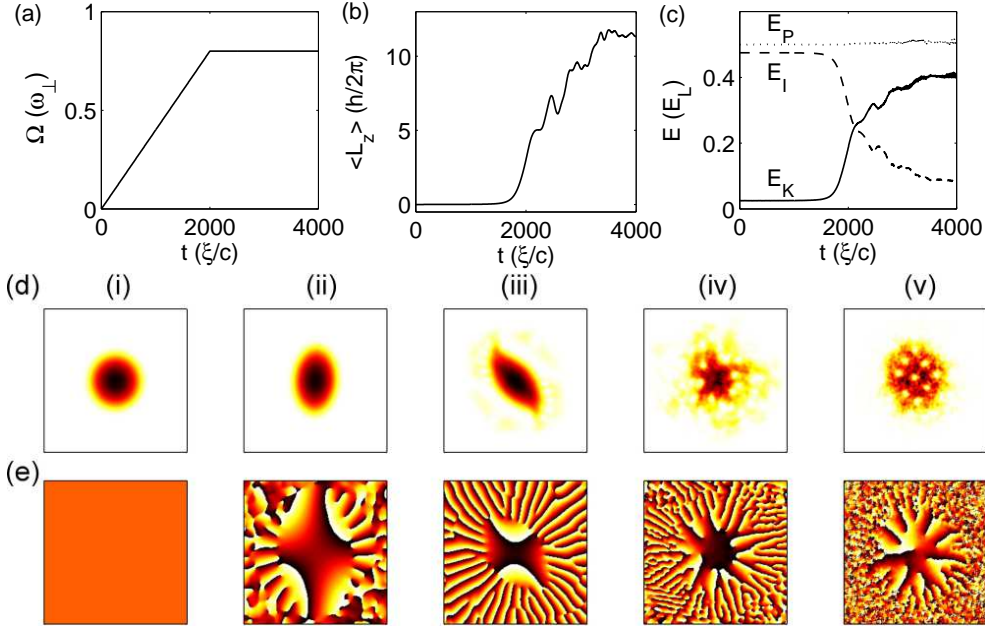
We have performed numerical simulations of the condensate while  $\Omega$  is adiabatically introduced. An example is presented in figure 3 for a fixed trap ellipticity of  $\epsilon = 0.05$ . The rotation frequency  $\Omega(t)$  is ramped up linearly from 0 to  $0.8\omega_\perp$  over a time of  $2000(\xi/c)$  and then maintained at a fixed value, as shown in figure 3(a).

Figure 3(e) shows snapshots of the condensate density during its evolution, while figure 3(f) shows the corresponding plots of the condensate phase. The condensate is initially circular in shape [figure 3(e)(i)] with a constant phase [figure 3(f)(i)]. As the rotation frequency is increased from zero, the condensate becomes elongated [figure 3e(ii)] as it traces out upper branch of the hydrodynamic solutions. The irrotational velocity field of equation (5) correspond to a phase profile  $\phi(x, y) \propto xy$  which is clearly evident in figure 3f(ii). On the outskirts of this irrotational phase pattern we see  $2\pi$  phase singularities. These are termed ‘ghost’ vortices because they cannot be seen in the density profile [14]. However, at some point the ‘ghost’ vortices penetrate the bulk of the condensate such that it begins to deviate from the smooth quadrupole solution [figure 3(e-f)(iii)], marking the onset of the dynamical instability. This instability disrupts the condensate into a turbulent state [figure 3(e)(iv)], which subsequently relaxes into a vortex lattice [figure 3(e)(v)] via vortex-sound interactions [18].

At early times, the  $z$ -component angular momentum per particle  $\langle \tilde{L}_z \rangle$  is zero, as shown in figure 3(b). However, when the instability kicks in angular momentum becomes rapidly driven into the system by the rotating trap, up to some maximum value. Figure 3(c) shows the evolution of the kinetic energy (solid line), interaction energy (dashed line) and potential energy (dotted line) during the dynamics. We have normalised these positive components of the energy by the laboratory frame energy  $E_L = (E_K + E_P + E_I)$ .

The condensate instability is associated with a sharp increase in the kinetic energy as the trap drives the condensate into an energetic turbulent state, and a decrease in





**Figure 3.** (a) The ramping up of the trap rotation frequency over time. (b) The average  $z$ -component angular momentum per particle during the simulation. (c) The evolution of the condensate kinetic energy (solid line), interaction energy (dashed line) and potential energy (dotted line) under the rotation frequency ramp shown in (a) and for a fixed trap ellipticity  $\epsilon = 0.05$ . (d) Snapshots of the condensate at (i)  $t = 0$ , (ii)  $t = 1775$ , (iii)  $t = 2320$ , (iv)  $t = 3670$ , and (v)  $t = 15000(\xi/c)$ . Each image is of dimension  $50\xi$  by  $50\xi$ , although the simulations were conducted in a numerical box of size  $100\xi$  by  $100\xi$ . (e) Corresponding snapshots of the condensate phase.

the interaction energy as the condensate becomes more diffuse.

Following the instability, the dynamics are explicitly time dependent and progress regardless of whether the trap frequency continues to be ramped up or is stopped. As such, we employ this characteristic time dependent deviation of the energies to define the point of condensate instability. In figure 3, for example, the instability kicks in at  $t \approx 1800(\xi/c)$ , corresponding to a rotation frequency of  $\Omega \approx 0.73\omega_{\perp}$ . With a very slow ramping rate this point can be pinpointed to very high accuracy and is more exact than in previous studies where the point of instability was determined ‘by eye’ [20].

Using the GPE we have mapped out the rotation frequency at which the condensate becomes unstable for a range of trap ellipticities and for two different ramping rates, with the results plotted in figure 4(a) (circles and squares). We find that the ramping rate can significantly affect the point at which the condensate breaks down. For  $\epsilon \leq 0.05$  we employ a ramping rate of  $d\Omega/dt = 2 \times 10^{-4}\omega_{\perp}^2$  (squares). Here the GPE shows that the condensate becomes unstable in the frequency range  $0.7\omega_{\perp} \lesssim \Omega \lesssim 0.8\omega_{\perp}$ , in good agreement with the boundary of the main dynamically unstable region (shaded region). For  $\epsilon \geq 0.04$  we employ a slower ramping rate of  $d\Omega/dt = 4 \times 10^{-6}\omega_{\perp}^2$  (circles). Here the GPE simulations show that the condensate instability sets in at much lower rotation frequencies ( $0.55\omega_{\perp} \lesssim \Omega \lesssim 0.6\omega_{\perp}$ ) that are consistent with the narrow band of dynamical instability. As discussed in section



(2) this narrow band of dynamical instability features small eigenvalues, and so the dynamical instability is slow to evolve. The simulations show that, providing the ramping rate is high enough, the condensate can pass through the narrow region of dynamical instability with negligible effect. Here we have not presented the slow ramping rate for ellipticities  $\epsilon < 0.04$  since the point of instability becomes less clear. Due to the weakened effect of the narrow instability region on the condensate (reduced eigenvalues and narrower width), the condensate passes through the narrow region of instability before becoming fully unstable. However it undergoes a partial instability that distorts the density slightly from its initially smooth profile. Upon emerging from this unstable region the condensate slowly relaxes to its steady state solution. When it reaches the second instability region the condensate breaks down fully. For slower ramping rates the condensate will break down fully within the narrow unstable region for  $\epsilon < 0.04$ . For the same reason our data for the high ramping rate is limited to ellipticities  $\epsilon \leq 0.05$ .

Madison *et al.* [7] adiabatically increased the rotation frequency at a fixed ellipticity of  $\epsilon \approx 0.028$  and observed the onset of condensate disruption at rotation frequency  $\Omega \approx 0.75\omega_{\perp}$ . This point, indicated on figure 4(a) by the cross, is in good agreement with the theoretical predictions, particularly the GPE results.

### 3.2. Procedure II

In this method the trap ellipticity is increased adiabatically from zero while the rotation frequency is kept fixed. Procedure II has been employed experimentally to generate vortices by Hodby *et al.* [5] and theoretically analysed using the hydrodynamic approach [12, 13] and GPE simulations [16, 20]. In these latter studies [16, 20], the GPE results were found to be in very good agreement with the hydrodynamic predictions and experimental results [5]. In particular, reference [20] elucidated the condensate instabilities that arise from Procedure II. Up to some critical ellipticity, the condensate accesses stable quadrupole solutions. However, once the critical ellipticity is reached the condensate becomes disrupted. There are three distinct regimes of instability depending on  $\Omega$ :

- *Ripple instability*  $\Omega < \Omega_b^0 < \omega_{\perp}/\sqrt{2}$ : The condensate follows the upper branch solutions to increasing values of  $\alpha$ , as indicated in figure 2 by the arrow labelled  $II(\Omega < \Omega_b^0)$ . However, at some critical ellipticity  $\epsilon_c$  the solutions become dynamically unstable according to equation (8). GPE simulations reveal that the dynamical instability manifests itself in the appearance and growth of density ripples, which ultimately lead to the complete disruption of the condensate.
- *Interbranch instability*  $\Omega_b^0 < \Omega < \Omega_x$ : The condensate follows the lower branch solutions to negative values of  $\alpha$  with increasing magnitude, as indicated by the arrow labelled  $II(\Omega > \Omega_b^0)$ . Eventually the lower branch ceases to be a solution. Since the upper branch solutions are stable the condensate tries to deform to the upper branch solutions, generating large unstable shape oscillations, which disrupt the condensate.
- *Catastrophic instability*  $\Omega > \Omega_x$ : As with the interbranch instability the condensate follows the lower branch solutions (route  $II(\Omega > \Omega_b^0)$  in figure 2). However, when the lower branch solution disappears, the upper branch is also unstable, and so no stable solutions exist. A large and sudden contortion of the condensate occurs, leading to a highly disrupted state.

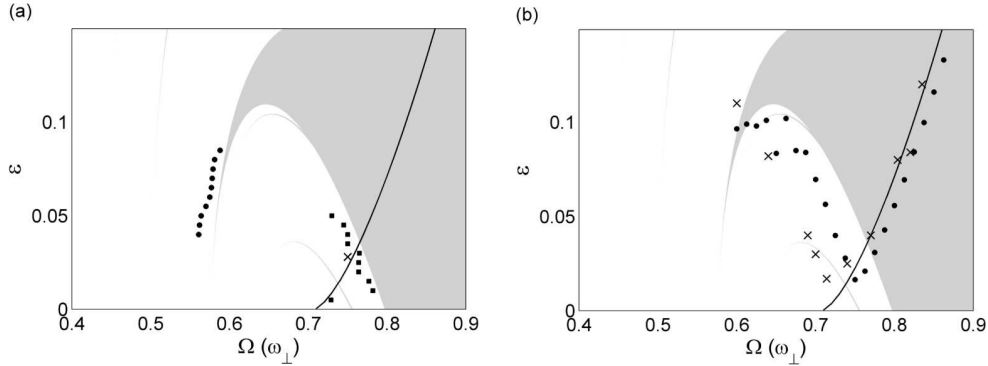


**Figure 4.** Phase diagrams in  $(\epsilon - \Omega)$  space showing the instability of a rotating elliptical condensate for (a) Procedure I (fixed  $\epsilon$  and increasing  $\Omega$ ). Squares represent the onset of instability according to the GPE simulations for a fast ramping rate of  $d\Omega/dt = 2 \times 10^{-4} \omega_{\perp}^2$ , while circles represent a slow ramping rate of  $d\Omega/dt = 4 \times 10^{-6} \omega_{\perp}^2$ . The cross is the experimental data from [7]. (b) Procedure II (fixed  $\Omega$  and increasing  $\epsilon$ ), the frequency of the bifurcation instability is given  $\Omega_b(\epsilon)$  (solid line). The crosses represent the experimental data of [5]. The dynamical instability (grey area) is shown in both plots.

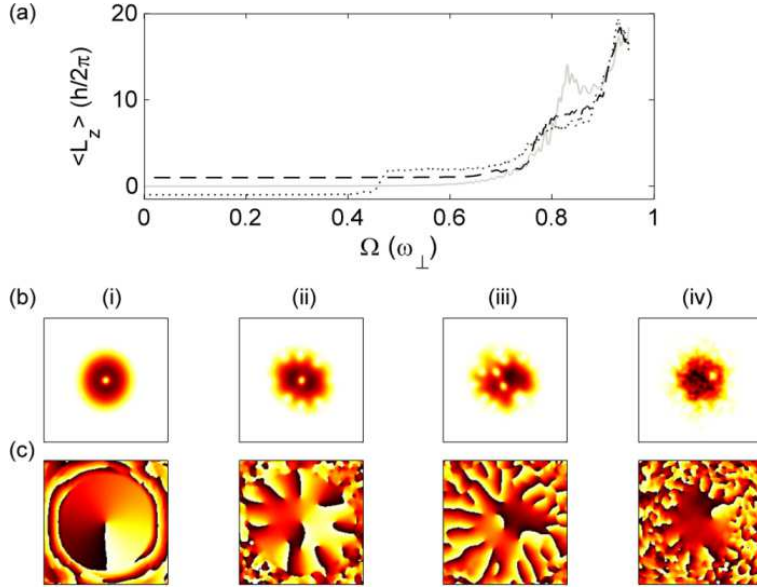
Each of these regimes leads to a turbulent state of vortices and sound waves, which relaxes into a vortex lattice via vortex-sound interactions [18].

Figure 4(b) maps out the point of the condensate instability in  $(\epsilon - \Omega)$  space under Procedure II. This figure is similar to figure 1(b) of reference [20], but employs an improved definition of the point of instability. Procedure II involves moving vertically upwards in  $(\epsilon - \Omega)$  space from the  $\epsilon = 0$  axis. Based on the hydrodynamic solutions and their dynamical stability, we expect that for  $\Omega < \Omega_X$  the condensate will become unstable when it reaches the bifurcation point (solid line) while for  $\Omega > \Omega_X$  the condensate will become unstable when it reaches the dynamically unstable region (shaded region).

We have performed GPE simulations of the condensate while the ellipticity is ramped up linearly, over a range of rotation frequencies. To ensure adiabaticity we employ a slow rate of change of ellipticity,  $d\epsilon/dt = 10^{-4} \omega_{\perp}$ . When the state of the condensate becomes explicitly time dependent, we have isolated the critical ellipticity. These GPE results, shown by the circles in figure 4(b), are in very good agreement with the hydrodynamic predictions, despite the assumptions of the hydrodynamic model. The experiment of Hodby *et al.* [5] performed Procedure II to investigate the instability of the condensate. The experimental results, shown by crosses in figure 4(b), are well-described by the both theoretical methods, particularly the GPE method.

#### 4. Rotating a condensate containing a vortex

We now consider the effect of rotating a condensate that already contains a singly-quantized vortex at its center. The hydrodynamic approach outlined in section 2.1 assumes a node-less Thomas-Fermi density profile and a quadrupolar velocity field. These approximations are no longer valid in the presence of a vortex, which creates a non-Thomas-Fermi node in the density and modifies the velocity field of the condensate. For this reason we proceed by solving the full GPE numerically, and make



**Figure 5.** Instability of a condensate containing a vortex following Procedure I with a fixed trap ellipticity of  $\epsilon = 0.085$ . (a)  $z$ -component angular momentum per particle  $\langle L_z \rangle$  as the rotation frequency  $\Omega$  is introduced in the presence of a vortex concurrent with (dashed line) and against (dotted line) the trap rotation. The results for a vortex-free condensate are also shown (grey line). (b) Density and (c) phase snapshots of the dynamics for the case of a vortex against the trap rotation. These snapshots correspond to rotation frequencies of (i)  $\Omega = 0.008\omega_{\perp}$ , (ii)  $\Omega = 0.46\omega_{\perp}$ , (iii)  $\Omega = 0.47\omega_{\perp}$  and (iv)  $\Omega = 0.54\omega_{\perp}$ .

comparisons to the non-vortex case which is understood analytically. In order to form the vortex state, we enforce a vortex phase profile  $\phi(x, y) = \tan^{-1}(y/x)$  during the imaginary time propagation method. A typical initial state is shown in figure 5(b)(i) and (c)(i).

#### 4.1. Procedure I

Using Procedure I, we rotate a condensate containing a vortex whose circulation is either concurrent with or against the trap rotation. Figure 5 presents the typical evolution of the condensate for a fixed trap ellipticity of  $\epsilon = 0.085$ . For the vortex-free condensate (grey line in figure 5), the growth of the angular momentum, which indicates the onset of instability, occurs at  $\Omega \approx 0.6\omega_{\perp}$ . When the vortex is concurrent with the trap rotation (dashed line), the angular momentum per particle is  $L_z = \hbar$  at early times. The onset of instability occurs at a higher frequency,  $\Omega \approx 0.65\omega_{\perp}$ . The instability progresses in a similar manner to the vortex-free case. ‘Ghost’ vortices develop on the condensate edge with the same flow direction as the initial vortex and the trap rotation. Eventually the state of the condensate becomes unstable. Once the instability starts, the growth of angular momentum occurs at a similar rate to the vortex-free case.

For the case of a vortex flowing against the trap rotation, the initial angular momentum is  $L_z = -\hbar$ . Once the trap rotation frequency is increased from zero, the

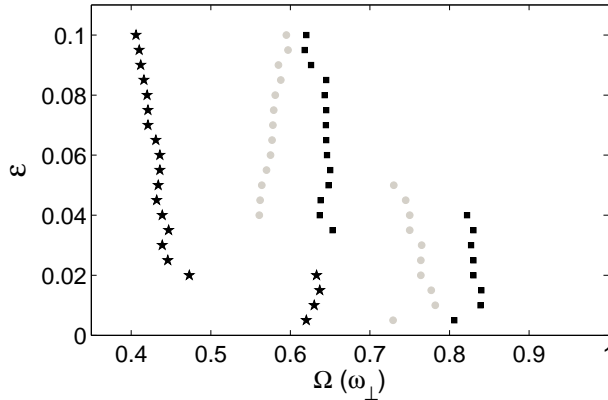


**Figure 6.** Instability of a condensate containing a vortex following Procedure I. Phase diagram in  $(\epsilon - \Omega)$  space showing the onset of condensate instability under Procedure I for a vortex concurrent with (squares) and against (circles) the trap rotation. The instability points for a vortex-free condensate are also presented (grey stars).

presence of this oppositely-rotating vortex is highly unfavourable in the system. At a relatively low frequency, which is  $\Omega \approx 0.4\omega_{\perp}$  for the example shown in figure 5(a), this configuration becomes dynamically unstable. Due to the highly unfavourable configuration, the instability progresses rapidly. ‘Ghost’ vortices appear on the condensate edge, whose circulation is concurrent with the trap rotation and in the *opposite* direction to the central vortex [see the density and phase images in figures 5(b)(ii) and (c)(ii)]. Their presence increases the angular momentum. Once the instability is reached, one or more ghost vortices become driven towards the condensate center [figures 5(a)(iii) and (b)(iii)]. For the example shown in figure 5 the opposing vortex becomes ejected from the condensate and the system settles into a configuration containing one concurrent vortex [figures 5(a)(iv) and (b)(iv)] and positive angular momentum of the order of unity. In other words, this initial phase of the instability has reversed the vortex configuration to the more stable, concurrent configuration. The system then progresses in this concurrent vortex state, remaining approximately stable until it reaches a second, higher critical frequency at  $\Omega \approx 0.7\omega_{\perp}$ . Angular momentum and multiple vortices becomes driven into the condensate and ultimately form a vortex lattice.

Using the GPE we have measured the onset of instability of Procedure I over a range of trap ellipticities, with the results presented in figure 6. We consider the case where the vortex flow is concurrent with (squares) and against (stars) the trap rotation. The results from section 3.1 for a vortex-free condensate are shown for comparison (grey circles). The behaviour of the critical rotation frequencies for each case is non-trivial. Crucially, however, the presence of the vortex shifts the critical frequencies. For a vortex concurrent with the rotation, the critical frequencies become shifted to higher values, while for a vortex against the rotation, the critical frequencies are shifted to lower frequencies.

In the absence of a vortex, the quadrupole mode of a condensate is predicted to become unstable at a rotation frequency  $\Omega = \omega_{\perp}/\sqrt{2}$  [28]. This assumes an axisymmetric system ( $\epsilon = 0$ ) in the Thomas-Fermi limit. In a similar manner, several

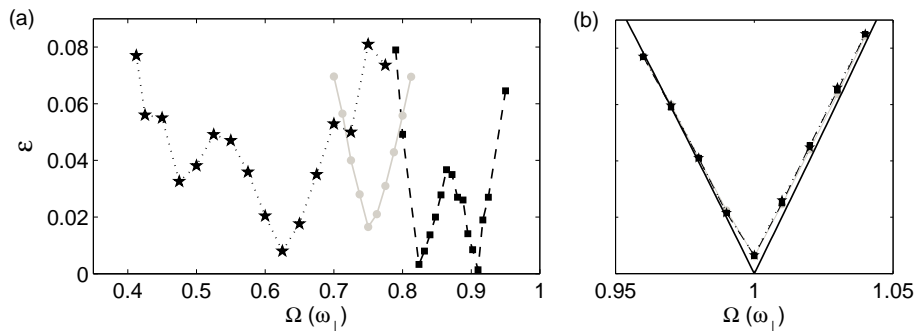


**Figure 7.** (a) Phase diagram in  $(\epsilon - \Omega)$  space showing the onset of condensate instability under Procedure II for a vortex concurrent with (squares) and against (stars) the trap rotation. The instability points for a vortex-free condensate are also presented (grey circles). (b) The centre-of-mass instability in the region  $\Omega \sim \omega_{x,y}$ , with the analytic prediction of  $\epsilon = \pm(1 - \Omega^2)$  shown (solid line) [12].

studies have theoretically considered the quadrupole mode of a condensate containing a vortex [23, 24, 25, 26]. It is predicted that the presence of the vortex shifts the critical frequency by  $\Delta\Omega = (7\hbar\omega_{\perp}/8\mu)$ . For the condensate parameters employed in this study ( $\mu = 7\hbar\omega_{\perp}$ ), this shift is  $\Delta\Omega = 0.125\omega_{\perp}$ , which is in good agreement with the observed shifts in figure 6.

#### 4.2. Procedure II

We now consider a condensate containing a vortex and following Procedure II. The critical ellipticities at which the condensate becomes unstable are mapped out in figure 7(a) for a vortex concurrent with (squares) and against the trap rotation (stars). The results from section 3.2 are shown for comparison (grey circles). Figure 7(b) is the region of the plot centered around the center of mass instability (where  $\Omega \approx \omega_{\perp}$ ). The solid line shows the theoretical position of the center of mass instability. All the cases (regardless of vortex configuration) break down at the same point, as predicted by the theory (as this phenomenon is classical, it depends only on the center of mass  $\langle \mathbf{x} \rangle$  and not on the quantum mechanical distribution of the wavefunction)

Again, the condensate instability is shifted to higher frequencies by the presence of a concurrent vortex and lower frequencies by the presence of an oppositely rotating vortex.

Although the presence of a vortex and its configuration within the BEC has a large effect on the stability of the system, once the BEC has become unstable its behaviour is similar in all cases. The kinetic energy's contribution to the total energy increases substantially whilst the contribution from the interaction energy becomes much less important. In all cases the instability allows vortices to enter the condensate, which ultimately settle into a lattice.

## 5. Conclusions

In this paper we have analysed and mapped out the instability of a condensate to a rotating elliptical trap, both in the absence and presence of a vortex in the initial condensate. We follow two methods of introducing the driving potential - Procedure I

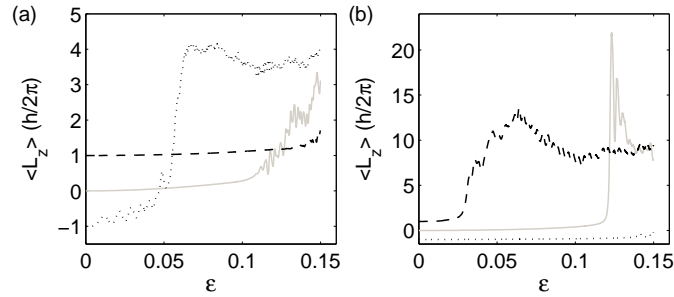


**Figure 8.** Angular momentum per particle  $\langle L_z \rangle$  as Procedure II is followed in the presence of a vortex concurrent with (dashed line) and against (dotted line) the trap rotation. The results for a vortex-free condensate are also shown (grey line). The rotation frequency is (a)  $\Omega = 0.6\omega_\perp$  and (b)  $\Omega = 0.85\omega_\perp$ .

involves increasing the rotation frequency at fixed trap ellipticity, while Procedure II involves increasing the trap ellipticity at fixed rotation frequency. These procedures are performed adiabatically so that the stable condensate accesses the quadrupolar static solutions in the rotating frame. In the vortex-free case, these can be analysed within the Thomas-Fermi limit using the classic hydrodynamic equations. At a critical rotation frequency/ellipticity, the solutions become unstable. We map out this point of instability using time-dependent simulations of the Gross-Pitaevskii equation. Although the non-vortex case has been examined in detail elsewhere, we present some additional data and demonstrate the good agreement with the hydrodynamic predictions and experimental data.

In the presence of a vortex, the points of instability become shifted. For a vortex which is concurrent with the trap rotation, the instability is shifted to higher rotation frequencies, while for a vortex which is against the trap rotation, the instability is shifted to lower rotation frequencies. The shift is of the order of  $0.1\omega_\perp$ , which is in good agreement with the shift of the quadrupole mode that is predicted to occur in the presence of a vortex.

## Acknowledgments

We acknowledge support from the University of Melbourne and the Australian Research Council. We thank C. J. Foot and E. Hodby for the use of experimental data.

## References

- [1] Fetter A L and Svidzinsky A A 2001 *J. Phys. Condens. Matter* **13** R135
- [2] Osborn D V 1950 *Proc. Phys. Soc. A* **63** 909
- [3] Madison K W, Chevy F, Wohlleben W and Dalibard J 2000 *Phys. Rev. Lett.* **84** 806
- [4] Abo-Shaer J R, Raman C, Vogels J M and Ketterle W 2001 *Science* **292** 476
- [5] Hodby E *et al.* 2001 *Phys. Rev. Lett.* **88** 010405
- [6] Haljan P C, Coddington I, Engels P, and Cornell E A 2001 *Phys. Rev. Lett.* **87** 210403
- [7] Madison K W, Chevy F, Bretin V and Dalibard J 2001 *Phys. Rev. Lett.* **86** 4443.
- [8] Raman C *et al.* 2001 *Phys. Rev. Lett.* **87** 210402
- [9] Lundh E, Pethick C J and Smith H 1997 *Phys. Rev. A* **55** 2126
- [10] Butts D A and Rokhsar D S 1999 *Nature* **397** 327

- [11] Feder D L, Clark C W, and Schneider B I 2000 *Phys. Rev. A* **61** 011601
- [12] Recati A, Zambelli F and Stringari S 2001 *Phys. Rev. Lett.* **86** 377
- [13] Sinha S and Castin Y 2001 *Phys. Rev. Lett.* **87** 190402
- [14] Tsubota M, Kasamatsu K, and Ueda M 2002 *Phys. Rev. A* **65** 023603; Kasamatsu K, Tsubota M and Ueda M 2003 *Phys. Rev. A* **67** 033610.
- [15] Penckwitt A A, Ballagh R J and Gardiner C W 2002 *Phys. Rev. Lett.* **89** 260402
- [16] Lundh E, Martikainen J P and Suominen K A 2003 *Phys. Rev. A* **67** 063604
- [17] Lobo C, Sinatra A, and Castin Y 2004 *Phys. Rev. Lett.* **92** 020403
- [18] Parker N G and Adams C S 2005 *Phys. Rev. Lett.* **95** 145301
- [19] Parker N G and Adams C S 2006 *J. Phys. B* **39** 43
- [20] Parker N G, van Bijnen R M W and Martin A M 2006 *Phys. Rev. A* **73** 061603(R)
- [21] Jackson B and Barenghi C F 2006 *Phys. Rev. A* **74** 043618
- [22] Dalfovo F, Giorgini S, Pitaevskii L P and Stringari S 1999 *Rev. Mod. Phys.* **71** 463
- [23] Zambelli F and Stringari S 1998 *Phys. Rev. Lett.* **81** 1754
- [24] Svidinsky A A and Fetter A L 1998 *Phys. Rev. A* **58** 3168
- [25] Krämer M, Pitaevskii L, Stringari S and Zambelli F 2002 *Laser Phys.* **12** 113
- [26] Williams J E, Zaremba E, Jackson B, Nikuni T and Griffin A 2002 *Phys. Rev. Lett.* **88** 070401
- [27] Rosenbusch P *et al.* 2002 *Phys. Rev. Lett.* **88** 250403
- [28] Stringari S 1996 *Phys. Rev. Lett.* **77** 2360
- [29] Castin Y and Dum R 1999 *Eur. Phys. J. D* **7** 399
- [30] Chevy F, Madison K W and Dalibard J 2000 *Phys. Rev. Lett.* **85** 2223; Hechenblaikner *Get al.* 2002 *Phys. Rev. Lett.* **88** 070406
- [31] Minguzzi A, Succi S, Toschi F, Tosi M and Vignolo P 2004 *Phy. Rep* **395** 223